

Two-Dimensional Condensation and Reorientation of the Bromide Salt of the Heptyl Viologen Cation Radical at the Hg/DMSO Interface

Juan Ignacio Millán, Rafael Rodríguez Amaro, Juan José Ruiz, and Luis Camacho*

Departamento de Química Física y Termodinámica Aplicada, Facultad de Ciencias, Universidad de Córdoba, Avda San Alberto Magno s/n, E-14004 Córdoba, Spain

Received: December 7, 1998; In Final Form: March 11, 1999

In DMSO containing Br^- ions, the heptyl viologen cation radical ($\text{HV}^{\bullet+}$) can form two different types of two-dimensional (2D) phase on Hg. Thus, $\text{HV}^{\bullet+}$ can take a planar conformation relative to the surface; however, depending on the applied potential, it can reorient itself to adopt a conformation where the bipyridine group lies edge-on or tilted relative to the electrode surface. We analyzed the structure and stability of the two phases and found $\text{HV}^{\bullet+}$ and Br^- ions to take part in a 1:1 ratio in both. We also studied the kinetics of formation of the two phases, as well as that of reorientation between them, and found both to involve two-dimensional nucleation and growth mechanisms.

Introduction

The stability of two-dimensional (2D) condensed phases of neutral organic molecules on an electrode has been analyzed in terms of the following equation^{1–3}

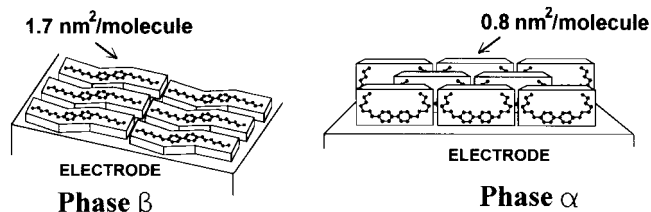
$$[\Delta E]^2 = ART \ln c + BT + C \quad (1)$$

where c is the adsorbate concentration, A , B , and C are constants, and ΔE , after Sridharan et al.,² is defined as the difference between E_t^+ and E_t^- , which are the positive and negative potential, respectively, by which the region where the condensed phase exists is bounded. Notwithstanding its approximate character,^{2–4} eq 1 is obeyed by a number of real-life systems.^{1–15} In a slightly modified form, this equation was used to interpret the formation of a 2D phase by guanidinium cations with nitrate anions in a 1:1 ratio.¹⁶ In eq 1, the concentration c substitutes for the product of the guanidinium and nitrate ion concentrations in the medium. In this way, De Levie et al.¹⁶ succeeded in describing the stability of the condensed phase in terms of a critical product that can be considered an interfacial analogue of the solubility product.

In any case, eq 1 has only been used under conditions where the condensed phase is in contact with a solution of the substance from which it is formed so that the chemical potential for the substance can readily be controlled. On the other hand, some organic species form 2D phases from their reduction products or intermediates. Such is the case with the cation radicals of 1,1-disubstituted 4,4'-bipyridinium salts or viologens, which form condensed phases on Hg in an aqueous medium.^{17–23} Equation 1 has never to date been applied to these 2D phases since, on one hand, the aqueous medium precludes the determination of E_t^- and, on the other, the concentration of the cation radical on the electrode surface depends on the applied potential.

In previous work,²⁴ the cation radical of heptyl viologen ($\text{HV}^{\bullet+}$) was found to form two different types of 2D phase on Hg in water/DMSO mixed solvents with a volume fraction $X_{\text{DMSO}} > 0.55$ in the presence of Br^- ions. At potentials between

SCHEME 1: Proposed Structures for Phases α and β (from Ref 24)



–300 and –350 mV, a phase is formed such that the surface concentration of $\text{HV}^{\bullet+}$, Γ_β , is about 1.04×10^{-10} mol/cm² (phase β in Scheme 1). In this phase, $\text{HV}^{\bullet+}$ molecules adopt a planar configuration relative to the electrode surface. At more negative potentials, a new phase is formed (phase α in Scheme 1) such that $\Gamma_\alpha \approx 2.08 \times 10^{-10}$ mol/cm² and the molecules adopt a more compact configuration than in the previous phase. In phase α , the plane containing the bipyridine group is edge-on or tilted relative to the electrode surface. Unfortunately, no specific model for the orientation of $\text{HV}^{\bullet+}$ can be established owing to the different possible conformations that the alkyl chains in the molecule can take.^{24,25} Scheme 1 provides a depiction of this phase in an edge-on configuration. One of the same type was previously proposed to account for the adsorption of the 4,4'-bipyridine cation radical on Ag in the presence of I^- ions.²⁶

The above-described phases α and β also occur in pure DMSO. In this work, we analyzed the experimental conditions under which the two are formed. In this solvent, the transition from phase β to phase α can take place either directly or through a potential zone where $\text{HV}^{\bullet+}$ is adsorbed on the electrode but forms no condensed phase. Also, pure DMSO allows one to identify the potentials that bound the region where each phase exists, and hence to check whether eq 1 is obeyed.

Experimental Section

Practical-grade 1,1'-diheptyl-4,4'-bipyridinium dibromide (purity grade, 97%) was purchased from Aldrich, and dimethyl sulfoxide (puriss p.a.), from Fluka. Both were used as received.

* E-mail: qf1cadel@lucano.uco.es.

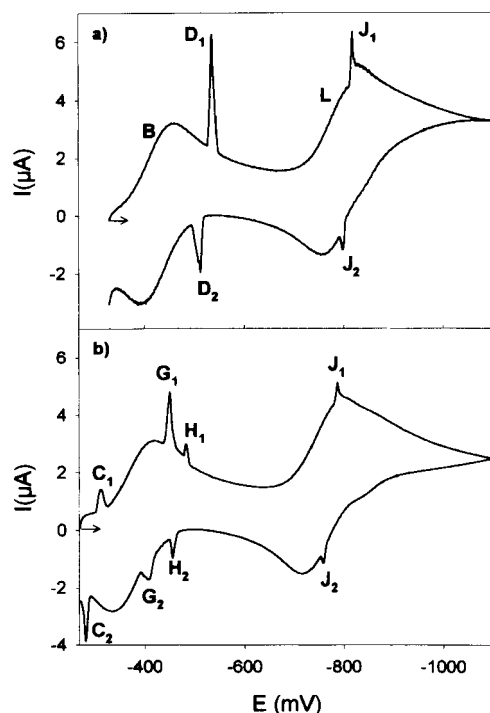


Figure 1. Cyclic voltammograms for 2 mM HV^{2+} in DMSO containing (a) 0.2 M KBr and (b) 0.04 M KBr, obtained at $T = 16^\circ\text{C}$ at $\nu = 100$ mV/s. The arrows show the initial potential and the scan direction.

All other chemicals were Merck analytical-grade reagents and also used without further purification.

Mercury was purified in dilute nitric acid and triply distilled in vacuo. The measuring cell was thermostated to within $\pm 0.1^\circ\text{C}$. Voltammetric measurements were made on a Quilceton electronic system. A static mercury drop electrode (SMDE) with an area of $1.86 \pm 0.05 \text{ mm}^2$ was used as the working electrode. A potential E_e was applied over an interval $t_e \approx 2 \text{ s}$ (equilibration time) and a cyclic voltammogram was then recorded between E_e and the final potential (E_f) in each run. Ag/AgCl and Pt wire were used as reference and auxiliary electrode, respectively. All measurements were made in a nitrogen atmosphere.

Capacitance–potential curves recorded by using a PAR M273 potentiostat with automatic correction for the iR drop, equipped with a PAR 5210 lock-in amplifier. The frequency and amplitude of ac modulation were fixed at 277 Hz and 10 mV, respectively. This instrumental setup was governed by M270 Research Electrochemistry Software.

Results

Figure 1 shows the voltammograms for 2 mM HV^{2+} in DMSO containing two different concentrations of KBr, obtained at a scan rate $\nu = 100$ mV/s at $T = 16^\circ\text{C}$.

In the presence of 0.2 M KBr (Figure 1a), HV^{2+} exhibits two well-defined peaks, **B** and **L**, which possess the typical features of diffusion-controlled processes and are due to the first and second one-electron reduction of HV^{2+} , respectively.²⁷ The scan to more negative potentials reveals two additional peaks, **D**₁ and **J**₁, which are sharp and narrow, consistent with the surface character of the electrode processes from which they arise. The anodic limit of the electrode in this medium is -330 mV, so the voltammogram was run above this potential. As in the previous case, in a medium containing 0.04 M KBr (Figure 1b), HV^{2+} gives peaks **B** and **L**. However, the anodic limit of the electrode in this medium is close to -270 mV, so an additional peak, **C**₁, which is masked in the voltammogram

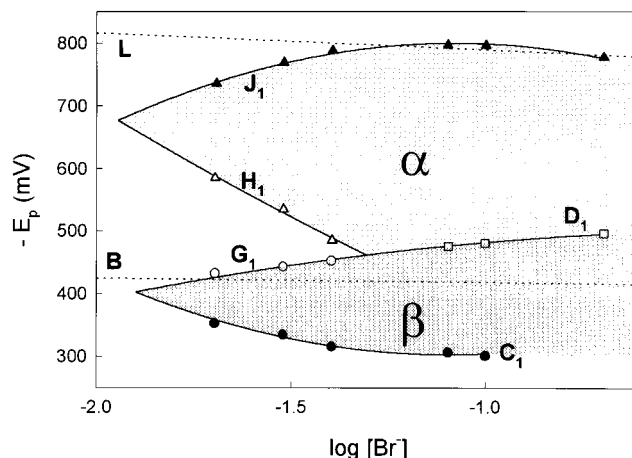


Figure 2. Plots of E_p vs $\log [\text{Br}^-]$ for 2 mM HV^{2+} in DMSO corresponding to peaks **C**₁ (●), **G**₁ (○), **D**₁ (□), **H**₁ (Δ), and **J**₁ (▲). The dotted line corresponds to **B** and **L** peaks and the shaded zones to the regions of occurrence of phases α and β . All other conditions as in Figure 1.

obtained in 0.2 M KBr, becomes apparent. Also, peak **D**₁ is split in two (**G**₁ and **H**₁). As in the previous case, peak **J**₁ is also obtained. The scans to more positive potentials provide sharp, narrow peaks related to the previous ones and designated with the same letters but subscript 2 instead of 1.

Figure 2 shows the variation of the peak potentials (E_p) against the logarithm of the Br^- ion concentration for the above-described peaks. The experimental conditions used were $[\text{HV}^{2+}] = 2 \text{ mM}$, $\nu = 100$ mV/s, and $T = 16^\circ\text{C}$.

In the figure, dotted lines represent the variation of E_p for peaks **B** and **L**. As regards the other peaks, **C**₁ and **H**₁ shift to more positive potentials with an increase in the salt concentration and the opposite is true of peaks **D**₁ and **G**₁. Peak **J**₁ exhibits a more complex behavior; in fact, it initially shifts to more negative potentials as the salt concentration is increased; at high enough salt concentrations, however, it shifts to slightly more positive potentials and appears very close to peak **L**. In a 0.01 M KBr medium, peaks **C**₁, **G**₁, **H**₁, and **J**₁ disappear simultaneously, so only peaks **B** and **L** are observed. Figure 2 also shows two shaded potential regions called α and β , the meaning of which is explained below. Peaks **C**, **D**, **G**, **H**, and **J** have been detected in media containing Br^- or I^- ions but never in the presence of NO_3^- , SO_4^{2-} , or Cl^- ions.

Increasing the HV^{2+} concentration while keeping all other variables constants (data not shown) had effects similar to those of raising the Br^- concentration (see Figures 1 and 2).

Figure 3 shows selected voltammograms obtained at $\nu = 100$ mV/s, at variable temperatures, for a 2 mM solution of HV^{2+} in DMSO containing 0.2 M KBr.

As regards adsorption peaks, only **D** and **J** are observed in the voltammograms recorded at $T = 16^\circ\text{C}$. At $T = 20^\circ\text{C}$, however, peak **D** is split into **G** and **H**, and peak **J** is also observed (Figure 3b). These three peaks are also observed at $T = 24^\circ\text{C}$ (Figure 3c); however, **G** and **J** are shifted to more positive potentials and **H** to more negative ones relative to the previous temperature. At $T = 45^\circ\text{C}$ (Figure 3d, solid line), peaks **H** and **J** disappear simultaneously; the voltammogram exhibits peak **G** and also peak **C**, which is masked by the narrow anodic limit of the electrode at lower temperatures. Finally, at $T = 57^\circ\text{C}$ (Figure 3d, dashed line), peaks **C** and **G** disappear concurrently. On the basis of the previous results, raising the temperature has the same effect on the adsorption peaks as lowering the Br^- or HV^{2+} concentration.

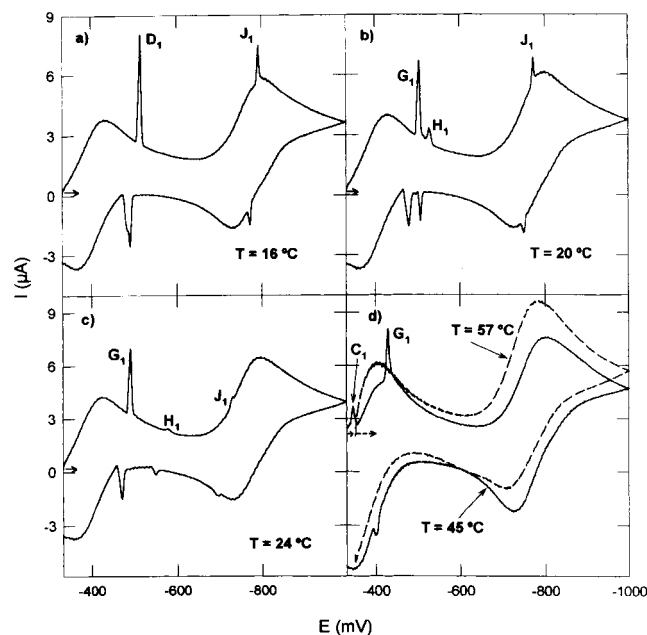


Figure 3. Cyclic voltammograms for 2 mM HV²⁺ in DMSO containing 0.2 M KBr, obtained at $T = 16$ °C (a), 20 °C (b), 24 °C (c), and 45 °C (d) (solid lines) and at 57 °C (dashed line). All other conditions as in Figure 1.

TABLE 1: Selected Q Values and Voltammetric Data for the Adsorption Peaks^a

peaks	Q ($\mu\text{C}/\text{cm}^2$)	$\partial \log I_p / \partial \log \nu$	$\partial \log W / \partial \log \nu$	$\partial \log \Delta E_p / \partial \log \nu$
C ₁ and C ₂	~10	0.63	0.39	0.37
D ₁	17–25	0.6	0.36	0.4
D ₂	10–15	0.6	0.36	0.4
G ₁	9–17	0.6	0.4	0.38
G ₂	7–9	0.6	0.4	0.38
H ₁ and H ₂	2–4	0.55	0.33	0.34
J ₁ and J ₂	1–5	0.64	0.3	0.37

^a The data are average values. The scan rate ranges between 25 and 250 mV/s.

Table 1 gives the amount of charge Q exchanged along each of the above-described peaks. Q values were obtained by integrating the peaks after eliminating the background current.

Note that only the values for the C peaks are roughly independent of the operating conditions. For the other peaks, Q decreases with decreasing concentration of HV and KBr, and also with increasing T , albeit in a nonlinear manner. Also worth noting are the marked changes in Q for peaks D₁ (17–25 $\mu\text{C}/\text{cm}^2$) and G₁ (9–17 $\mu\text{C}/\text{cm}^2$), and the fact that these values diverge from those for D₂ (10–15 $\mu\text{C}/\text{cm}^2$) and G₂ (7–9 $\mu\text{C}/\text{cm}^2$).

We analyzed the nature of peaks C, D, G, H, and J by examining the changes in peak currents (I_p) and peak widths at half-height (W) with the scan rate (ν). The plots of $\log I_p$ against $\log W$ and $\log \nu$ were roughly linear for all peaks; the slopes are given in Table 1. We also analyzed the hysteresis or separation between peak potentials, $\Delta E_p = E_p(\text{X}_2) - E_p(\text{X}_1)$, where X denotes any of the peaks (C, D, G, H, or J). The plots of $\log \Delta E_p$ versus $\log \nu$ were all linear; their slopes are listed in Table 1. It should be noted that these data are average values for several experiments conducted under different operating conditions. Also, at least 10 voltammetric runs were performed over the scan rate range 25–250 mV/s, in each experiment.

In previous work,^{28,29} various criteria for characterizing 2D phase transitions on electrodes by cyclic voltammetry were

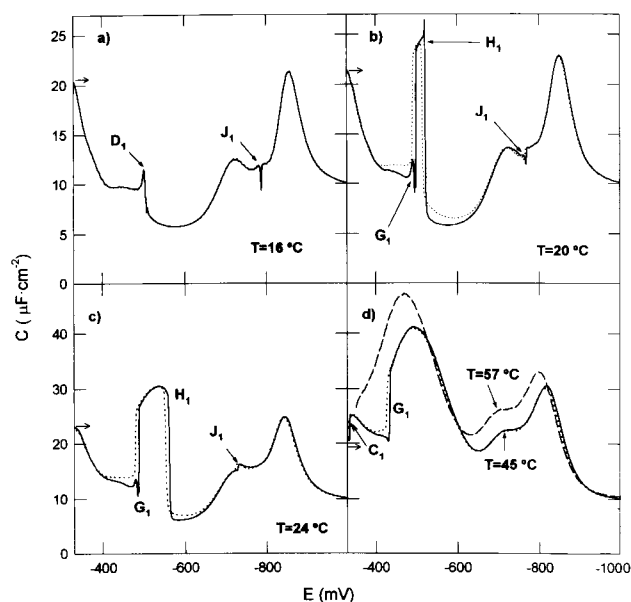


Figure 4. Capacitance (C) vs potential (E) curves obtained at $T = 16$ °C (a), 20 °C (b), 24 °C (c), and 45 °C (d) (solid lines) and at 57 °C (dashed line). The dotted line represents the C – E curves obtained in the scan to more positive potentials. C was determined at a frequency of 277 Hz and a scan rate of 2 mV/s, using a 10 mV pulse. All other conditions as in Figure 3.

derived. Thus, the log–log plots of I_p , W , and ΔE_p as a function of ν must all be linear and have slopes of x , $1 - x$, and $1 - x$, respectively, where $x \geq 0.6$. In the ideal situation (viz., a high nucleation rate and a low scan rate), $x = 0.6$.²⁸ In any case, x must fit experimental parameters equal to or slightly greater than 0.6.^{28,30,31}

On the basis of the previous criteria and on the experimental data of Table 1, one should be able to assign the five peaks studied to 2D phase transitions. To confirm this assumption and characterize the regions of occurrence of the phases involved, we ran capacitance–potential (C – E) curves under different conditions. Figure 4 shows some such curves, obtained at a variable temperature for a 2 mM HV solution containing 0.2 M KBr.

At $T = 16$ °C (Figure 4a), the capacitance initially decreases as the potential becomes more negative. Over the potential range from -400 to -500 mV, C is roughly constant. At $E \approx -500$ mV, C exhibits an abrupt jump coinciding with the appearance of peak D₁ in the voltammogram (see Figure 3a). At more negative potentials, C is again roughly constant (to about 6 $\mu\text{F}/\text{cm}^2$). Below -625 mV, C rises to a maximum. At $E \approx -800$ mV, C exhibits a new abrupt jump coinciding with the appearance of peak J₁ in the voltammogram. Finally, below -800 mV, C rises to a new maximum.

At $T = 20$ °C, peak D is split in two (G and H, Figure 3b). This results in an abrupt change in the C – E curves. The solid line in Figure 4b (scan to negative potentials) shows the curve obtained at 20 °C, which, as can be seen, is similar to the previous one except that, coinciding with the appearance of peak G₁, C exhibits an abrupt oscillation and a subsequent sharp increase (to values in the region of 25 $\mu\text{F}/\text{cm}^2$). The capacitance remains roughly at that level until it again decreases abruptly (to about 6 $\mu\text{F}/\text{cm}^2$) as peak H₁ appears in the voltammogram. The broken line in Figure 4b is the C – E curve obtained in the scan to positive potentials. As can be seen, there are clear signs of hysteresis in the regions where C changes in an abrupt manner. This in turn suggests the occurrence of phase transition phenomena.^{11,16} At $T = 24$ °C (Figure 4c), the high-capacitance

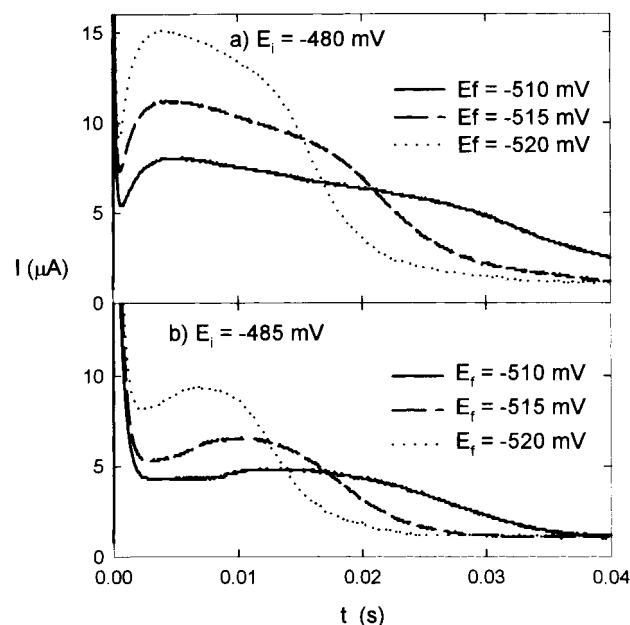


Figure 5. $I-t$ curves obtained for 1 mM HV solution containing 0.2 M KBr at $T = 16\text{ }^{\circ}\text{C}$. The potential applied before the potential jump (E_i) was held for 1 s. E_i and the final potential (E_f) for each curve are shown in the figure. The curves shown correspond to the appearance of peak G_1 in the voltammogram.

region ($25\text{--}30\text{ }\mu\text{F}/\text{cm}^2$) that spans the potentials of appearance of peaks **G** and **H** is broader than at the previous temperature, consistent with the greater distance between the voltammetric peaks (see Figure 3c). As can be seen, there is also marked hysteresis in the regions where the capacitance undergoes an abrupt change, between the forward (solid line) and reverse scan (dotted line).

At $T = 45\text{ }^{\circ}\text{C}$ (Figure 4d, solid line), the jumps in peaks **H** and **J** disappear, coinciding with the disappearance of the corresponding peaks in the voltammogram (see Figure 3d, solid line). Also, two jumps are clearly observed at the potentials of appearance of C_1 and G_1 . Finally, at $T = 57\text{ }^{\circ}\text{C}$, the voltammogram exhibits diffusion peaks only (see Figure 3d, broken line), consistent with the complete absence of jumps from the $C-E$ curves (Figure 4d, solid line). All capacitance curves virtually coincide with the curve for the supporting electrolyte at potentials below -1000 mV ; this suggests that the neutral form of HV is not adsorbed.

The $C-E$ curves of Figure 4 reveal a direct relationship between the jumps observed and the voltammetric peaks due to phase transition phenomena.

Two-dimensional phase transitions have also been studied by using the chronoamperometric technique.^{32,33} $I-t$ curves exhibit typical maxima that allow the nucleation processes involved to be characterized. We ran potentiostatic curves for peaks C_1 , D_1 , G_1 , H_1 , and J_1 . The curves were experimentally obtained by applying a potential E_i preceding the appearance of each peak for 1 s, followed by a potential pulse up to a potential E_f immediately following the appearance of the peak concerned. The $I-t$ curves for peaks C_1 , H_1 , and J_1 exhibited a single maximum, thus confirming the previous assignment of peaks (data not shown). However, the curves for peaks D_1 and H_1 were rather complex. Figure 5 shows the $I-t$ curves for peak G_1 obtained for a 1 mM solution of HV containing 0.2 M KBr at $T = 16\text{ }^{\circ}\text{C}$.

Figure 5a corresponds to a transition from $E_i = -480\text{ mV}$ to different E_f values. As can be seen, the current exhibits a first component (charging current) that drops to zero within the first

few milliseconds and is independent of the applied potential E_f , in addition to a second component that is E_f -dependent. The second component appears to result from the combined contributions of two different processes. Integration of these curves following removal of the charging current allowed us to calculate the amount of charge exchanged, viz., $14\text{ }\mu\text{C}/\text{cm}^2$, which is consistent with the value obtained by integrating the voltammetric peak under the same experimental conditions.

Figure 5b shows the $I-t$ curves obtained under the same operating conditions as the previous ones but using an initial potential $E_i = -485\text{ mV}$. At such a potential, the phase transition takes place, but at a slow pace; as a result, the process does not develop to completion within the time E_i is applied (viz., 1 s). Subsequently, the pulse to a potential E_f is applied and $I-t$ curves of the type shown in the figure are obtained. As can be seen, the shapes of the curves are quite simple and typical of 2D phase transitions.^{32,33} The amount of charge exchanged, as computed by integrating these curves, is about $6\text{ }\mu\text{C}/\text{cm}^2$. The $I-t$ curves for peak D_1 behave identically with the above-described ones for peak G_1 .

Assignment of Peaks and Characterization of 2D Phases

Before any peaks are assigned, we should underline the relationship between **C** and **G** on one hand, and **H** and **J** on the other; in fact, the peaks in each pair are always observed concurrently in the voltammograms. This provides additional evidence that these peaks correspond to phase transitions. In fact, each peak pair can be related to E_1^+ and E_1^- (the potentials that bound the region where a 2D phase is formed and destroyed).

Peaks C_1 and C_2 . These peaks, which were previously observed elsewhere, are given by HV^{2+} in mixed water/DMSO solvents with an DMSO volume fraction above 0.55.²⁴ The charge resulting from their integration, ca. $10\text{ }\mu\text{C}/\text{cm}^2$ (see Table 1), coincides with that observed in water/DMSO mixtures.²⁴ These peaks can be assigned to the formation (C_1) and destruction (C_2) of phase β . At the potentials of appearance of **C**, the dication, HV^{2+} , is the dominant species on the electrode surface, so the formation of phase β entails the reduction of about $1.04 \times 10^{-10}\text{ mol}/\text{cm}^2$,²⁴ which is responsible for the charge obtained on integration of the voltammetric peak.

Peaks D_1 and D_2 . These peaks were also previously observed and have been related to the reorientation of HV^{+} from phase β (at potentials more positive than those of the appearance of these peaks) to phase α (at potentials more positive than those of the appearance of the peaks). However, these peaks behave anomalously in that the charges they provide on integration are not coincident and that they are strongly dependent on the operating conditions (see Table 1). In the potential region where these peaks occur, the cation radical, HV^{+} , is the dominant species on the electrode surface since peak D_1 appears at more negative potentials than does **B**. Consequently, phase α (peak D_1), which is more compact than phase β , must be formed from HV^{+} molecules around the electrode and hence without the need to reduce further dication molecules. These peaks must therefore be small and result from a purely capacitive process (i.e., the charge associated with the **D** peaks must be much smaller than the experimentally observed value).

In water/DMSO mixtures with a volume fraction of the organic solvent $X_{\text{DMSO}} < 0.75$, peak D_1 appears at more positive potentials than peak **B** (see Figure 2 in ref 24). In these media, integration of D_1 and D_2 yields constant charge values close to $10\text{ }\mu\text{C}/\text{cm}^2$. Under these conditions, the dication is the dominant species around the electrode, so the formation of phase α entails

the prior reduction of additional HV²⁺ molecules, which is responsible for the charge observed. The increased size of the **D** peaks in pure DMSO relative to those obtained in mixtures with $X_{\text{DMSO}} > 0.75$ is thus surprising.

One possible explanation for this phenomenon is as follows: phase β formed by HV^{•+} may adsorb HV²⁺ molecules, thereby delaying the reduction of adsorbed molecules relative to unadsorbed HV²⁺, similarly to the phenomenon that produces adsorption post-waves.³⁴ In other words, peak **D**₁ must be due to the reorientation of phase β to phase α ; however, the charge for this peak obtained in pure DMSO must be assigned to the reduction of HV²⁺ molecules adsorbed on it, which are desorbed when the phase is destroyed. On the other hand, peak **D**₂ must be the result of the transition from phase α to phase β , which, again, can adsorb HV²⁺ molecules; however, only HV^{•+} molecules will be found in the vicinity of the electrode, molecules which will thus have to be oxidized. The extent to which HV²⁺ is adsorbed on phase α must be a function of the operating conditions judging by the fact that integration of these peaks yields variable amounts of charge (see Table 1). The $I-t$ curves of Figure 5 seemingly support the previous hypothesis.

Peaks G₁ and G₂. These peaks can be related to the destruction (**G**₁) and formation (**G**₂) of phase β ; in this case, however, the destruction of phase β , does not involve the formation of phase α , as can be inferred from the abrupt rise in capacitance between peaks **G** and **H** (see Figure 4). In the potential region between **G** and **H**, HV^{•+} may be adsorbed on the Hg electrode surface; however, the adsorption must take place in a random manner rather than through an organized structure. The charge observed along these peaks arises from the same source as that for the **D** peaks.

Domain of Phase β . The domain of phase β is the potential region between the **C** and **G** peaks (or that between the **C** and **D** peaks when the **G** and **H** peaks are overlapped). Figure 2 depicts such a region (shaded area β). Frequently, the β region reaches a plateau or potential zone where the capacitance is roughly constant; occasionally, however, the plateau is ill-defined (see Figure 4). One should bear in mind that the **B** peak always occurs between the **C** peaks and the **G** or **D** peaks (see Figure 2), so the capacitance values measured in this region may be affected by the simultaneous occurrence of this process.

Peaks H₁ and H₂. These peaks are due to the formation (**H**₁) and destruction (**H**₂), respectively, of phase α . The small charge obtained from their integration (about 2–4 $\mu\text{C}/\text{cm}^2$) must arise from a purely capacitive phenomenon. In fact, at the potentials of appearance of both peaks, the dominant species in the vicinity of the electrode is HV^{•+}, so phase α is formed or destroyed in the absence of a Faradic process.

Peaks J₁ and J₂. These two peaks can be assigned to the destruction (**J**₁) and formation (**J**₂), respectively, of phase α . As in the previous case, the small charge obtained upon integration (about 1–5 $\mu\text{C}/\text{cm}^2$) must be related to a purely capacitive phenomenon; however, the charge for these peaks increases as they shift to more negative potentials and approach the diffusion peak **L**, which results from the second one-electron transfer in HV²⁺. When peaks **J**₁ and **L** are close enough, the destruction of phase α (peak **J**₁) causes an abrupt increase in concentration of the cation radical around the electrode; as a result, a sizable fraction of its molecules are immediately reduced, which causes the observed charge increase.

Domain of Phase α . The domain of this phase is the potential region spanning the **D** and **J** peaks or the **H** and **J** peaks when the **D** peak is split into the **G** and **H** peaks. Such a region is represented by the shaded zone in Figure 2. It exhibits a

capacitance plateau ($C \approx 6 \mu\text{F}/\text{cm}^2$) at potentials close to –600 mV (Figure 4), whichever the HV and KBr concentrations, and the temperature. The increase in C at potentials more negative than those of appearance of the plateau but still within the α region can be related to the nearness to the diffusion peak **L** (see Figure 1).

Structure of the Phases

To analyze the composition of the 2D phases formed, a series of experiments involving checking whether the following equation held in each case were conducted:

$$[\Delta E]^2 = ART \ln [\text{HV}^{\bullet+}][\text{Br}^-] + BT + C \quad (2)$$

This equation coincides with eq 2 in ref 16 except that the guanidinium and nitrate ion concentrations have been replaced with the product of the HV^{•+} and Br[–] concentrations. Equation 2 allows one to define the widths $\Delta E_\alpha = E_\alpha^+ - E_\alpha^-$ and $\Delta E_\beta = E_\beta^+ - E_\beta^-$, where E_α^+ , E_α^- , E_β^+ , and E_β^- are the positive and negative potentials that bound the region where each phase occurs.

Structure of Phase β . The region where this phase exists is represented by the shaded zone β in Figure 2. For simplicity, we shall henceforward assume that, when the **G** and **H** peaks are overlapped, the properties of **G**₁ are similar to those of **D**₁. Accordingly, we shall use **G**₁ to refer to both **G**₁ and **D**₁. The formation (**C**₁) or destruction (**G**₁) of phase β is not characterized by the peak potentials for these processes, but rather by their standard potentials, E_C^0 and E_G^0 . These can be determined from the relation $E^0 = E_p + W/0.5263$,²⁸ where E_p and W are the peak potential and peak width at half-height, respectively. In theory, the difference between E_C^0 and E_G^0 could be used as a direct measure of ΔE_β . This is not true, however, since the HV^{•+} concentration undergoes an abrupt change in the β region. At any potential E , such a concentration can be calculated by using

$$[\text{HV}^{\bullet+}] = \frac{[\text{HV}^{2+}]_B}{1 + \exp\left(\frac{F(E - E_B^0)}{RT}\right) + \exp\left(-\frac{F(E - E_L^0)}{RT}\right)} \quad (3)$$

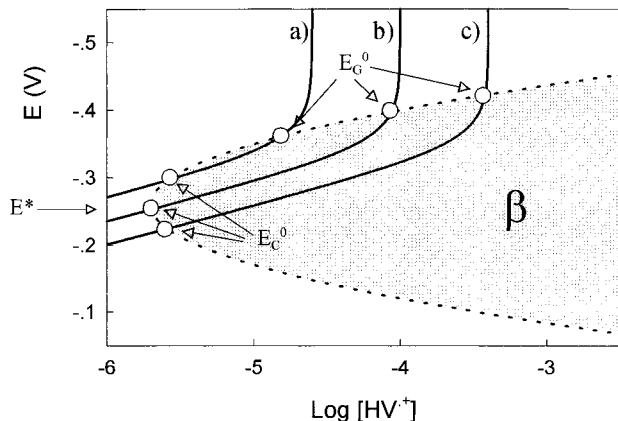
where $[\text{HV}^{2+}]_B$ is the concentration of HV²⁺ in the bulk solution and E_B^0 and E_L^0 are the standard reduction potentials of the HV²⁺/HV^{•+}, and HV^{•+}/HV couple, respectively, which can be estimated in each experiment from the intermediate potential between the peak potentials for peaks **B** or **L** and its corresponding oxidation peaks. Scheme 2 shows the variation of $\ln [\text{HV}^{\bullet+}]$ with E as per eq 3 at different $[\text{HV}^{2+}]_B$ values (curves a–c), with $E_B^0 = -350$ mV, $E_L^0 \ll E$, and $T = 16$ °C.

For a condensed phase, ΔE_β can be expressed in an alternative manner by using the equation $\Delta E_\beta = 2(E^* - E_\beta^-)$, where E^* is the maximum adsorption potential, which is roughly independent of the concentration and temperature.^{1,2} Also, when $\Delta E_\beta = 0$ in eq 2, one can define the critical product $K_C^* = [\text{HV}^{\bullet+}][\text{Br}^-] = \exp[(-B/AR) - (C/ART)]$ that must be reached for the phase to be formed.¹⁶ By combining these definitions with eq 2, one obtains

$$(E_\beta^+ - E_\beta^-)^2 = 4(E^* - E_\beta^-)^2 = ART \ln \left(\frac{[\text{HV}^{\bullet+}][\text{Br}^-]}{K_C^*} \right) \quad (4)$$

The shaded zone in Scheme 2 represents the region of occurrence of a generic condensed phase (β) as per eq 4 when T and $[\text{Br}^-]$ are assumed to be constant. The parameters used

SCHEME 2: Shaded Zone (β) Corresponding to the Region Where a 2D Phase Exists^a and Solid Lines Corresponding to the Predictions of Eq 3^b



^a Its bounds, E_{β}^{+} and E_{β}^{-} , were calculated from eq 4, using $[\text{Br}^{-}] = 0.1 \text{ M}$, $E^{*} = -260 \text{ mV}$, $K_{\text{C}}^{*} = 2 \times 10^{-7} \text{ M}^2$, and $\text{ART}/4 = 0.01 \text{ V}^2$. ^b With $E_{\text{B}}^{0} = -350 \text{ mV}$, $T = 16 \text{ }^{\circ}\text{C}$, and $[\text{HV}^{2+}]_{\text{B}} = 10^{-5} \text{ M}$ (a), 10^{-4} M (b), and 10^{-3} M (c).

to define the phase are given in the scheme footnote. The bounds of the shaded region are the two solutions, $E_{\beta}^{+} > E^{*}$ and $E_{\beta}^{-} < E^{*}$, to eq 4 at a given $[\text{HV}^{2+}]$ value. The condensed phase exists provided the concentration of the cation radical (solid lines in Scheme 2) at a given potential lies within the shaded zone. Therefore, the intersections of the solid lines with the shaded zone are the potentials E_{C}^{0} and E_{G}^{0} (see Scheme 2) that bound the region where the condensed phase for a given set of $[\text{HV}^{2+}]_{\text{B}}$, $[\text{Br}^{-}]$, and T values occurs. However, as can be seen from Scheme 2, depending on the relative values of the parameters, E_{C}^{0} can be more positive (curve c) or negative (curve a) than E^{*} . In physical terms, when $E_{\text{C}}^{0} < E^{*}$, phase β does not exist at the maximum adsorption potential E^{*} , where $[\text{HV}^{2+}][\text{Br}^{-}] < K_{\text{C}}^{*}$. In this case, the solutions to eq 4 correspond to two values of $E_{\beta}^{-} < E^{*}$ at two different concentrations of the cation radical.

We carried out two different experiments at $T = 16 \text{ }^{\circ}\text{C}$. In one, $[\text{HV}^{2+}]$ was kept constant at 2 mM while $[\text{Br}^{-}]$ was changed between 0.01 and 0.02 M; in the other, $[\text{Br}^{-}]$ was kept constant at 0.1 M and $[\text{HV}^{2+}]$ was varied over the range 2–0.4 mM. In all cases, E_{C}^{0} and E_{G}^{0} were calculated and substituted into eq 3 to obtain the concentration of HV^{2+} . Figure 6 shows the variation of E_{C}^{0} and E_{G}^{0} with $\ln([\text{HV}^{2+}][\text{Br}^{-}])$.

As can be seen, E_{C}^{0} and E_{G}^{0} shifted to more negative values with an increase in the $[\text{HV}^{2+}][\text{Br}^{-}]$ product, so $E_{\text{G}}^{0} < E^{*}$ and $E_{\text{C}}^{0} < E^{*}$ (see curve a in Scheme 2), and E_{C}^{0} and E_{G}^{0} are therefore two solutions, at different concentrations, to the following equation:

$$E_{\beta}^{-} = E^{*} - \sqrt{\frac{\text{ART}}{4}} \sqrt{\ln \frac{[\text{HV}^{2+}][\text{Br}^{-}]}{K_{\text{C}}^{*}}} \quad (5)$$

On the basis of this assumption, we fitted the data of Figure 6 to eq 5 using a numerical procedure. The parameter values thus obtained were $E^{*} = -232 \text{ mV}$, $K_{\text{C}}^{*} = 1.95 \times 10^{-6} \text{ M}^2$, and $A = 1.95 \times 10^{-5} \text{ V}^2/(\text{J}\cdot\text{mol})$. The solid line in Figure 6 shows the predictions of eq 5 for these parameters. The consistency between the experimental data and the predictions of eq 5 confirms both that $E_{\text{C}}^{0} < E^{*}$ and that the Br^{-} ion takes part, in a 1:1 ratio to species HV^{2+} , in the condensed phase.

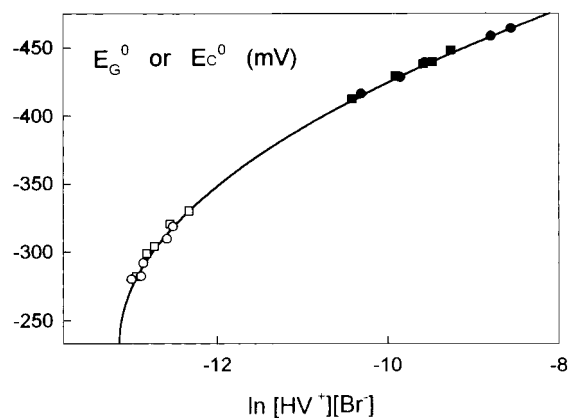


Figure 6. Plots of E_{C}^{0} and E_{G}^{0} vs $\ln([\text{HV}^{2+}][\text{Br}^{-}])$. The data shown were experimentally obtained. In one of the plots, the HV^{2+} concentration was 2 mM and the Br^{-} concentration was varied over the range 0.1–0.02 M [(○) E_{C}^{0} , (●) E_{G}^{0}]. In the other, the KBr concentration was kept at 0.1 M while that of HV^{2+} was changed from 2 to 0.4 mM [(□) E_{C}^{0} , (■) E_{G}^{0}]. The temperature was 16 $^{\circ}\text{C}$ in every case. The solid line represents the predictions of eq 5 with $E^{*} = -232 \text{ mV}$, $K_{\text{C}} = 1.95 \times 10^{-6} \text{ M}^2$, and $A = 1.95 \times 10^{-5} \text{ V}^2/(\text{J}\cdot\text{mol})$.

In addition to the experiments at a constant temperature of Figure 6, we conducted others at a variable T . In some experiments, $[\text{Br}^{-}]$ and $[\text{HV}^{2+}]$ were kept constant at 0.08 M and 2 mM, respectively, while T was varied over the range 16–40 $^{\circ}\text{C}$; in the others, $[\text{Br}^{-}]$ and $[\text{HV}^{2+}]$ were fixed at 0.04 M and 2 mM, respectively, while T was changed from 16 to 30 $^{\circ}\text{C}$. In all experiments, E_{C}^{0} and E_{G}^{0} were calculated, as were their corresponding cation radical concentrations, using the above-described procedure. The data set thus obtained was used to test the following equation:

$$(E_{\beta}^{-} - E^{*})^2 = \frac{\text{ART} \ln[\text{HV}^{2+}][\text{Br}^{-}] + BT + C}{4} \quad (6)$$

with the previously determined E^{*} value (−232 mV). The parameter values obtained by numerical fitting to eq 6 where $A = (1.97 \pm 0.02) \times 10^{-5} \text{ V}^2/(\text{J}\cdot\text{mol})$, $B = (-1.33 \pm 0.09) \times 10^{-3} \text{ V}^2/\text{K}$, and $C = 1.00 \pm 0.04 \text{ V}^2$. Figure 7 shows the variation of $[E_{\beta}^{-} - E^{*}]^2$ with $\{\text{ART} \ln([\text{HV}^{2+}][\text{Br}^{-}]) + BT + C\}/4$. In the figure, circles and squares represent E_{β}^{-} values equal to E_{C}^{0} and E_{G}^{0} , respectively.

As can be seen, the curves are reasonably linear, so eq 6 is acceptably satisfied.

Structure of Phase α . Parameter ΔE_{α} was determined from the distance between the peak potentials for \mathbf{H}_1 and \mathbf{J}_1 , which entailed relating the peak potential for \mathbf{H}_1 with E_{α}^{+} and that for \mathbf{J}_1 with E_{α}^{-} . The ΔE_{α} values thus obtained were virtually identical with those found by measuring the distance between the standard potentials for the two peaks, $E_{\text{H}}^{0} - E_{\text{J}}^{0}$. This coincidence was the result of the shifts in the $E_{\text{p}} - \nu$ curves being similar for all peaks (see Table 1), which canceled the influence of ν in subtracting. This method for measuring ΔE was used in previous work.¹⁴

However, some caution must be exercised in applying eq 2 to the ΔE_{α} values thus obtained. Thus, when peaks \mathbf{G}_1 and \mathbf{H}_1 join to give peak \mathbf{D}_1 , the E_{p} value for this last is dictated by the destruction of phase β rather than that of phase α , as can be inferred from the fact that \mathbf{D}_1 changes identically with \mathbf{G}_1 (see Figure 2). For this reason, the E_{p} values for peak \mathbf{D}_1 cannot be used to define the thermodynamic value of ΔE_{α} . Also, we applied eq 2 to results from experiments where the peak potential

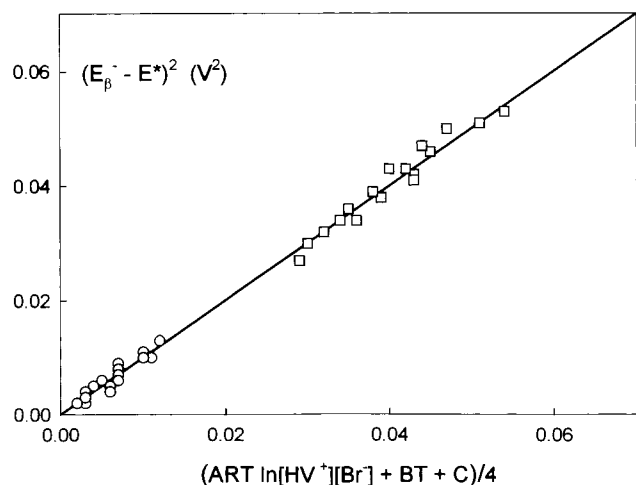


Figure 7. Plots of $[E_\beta - E^*]^2$ vs $\{ART \ln([HV^{2+}][Br^-]) + BT + C\}/4$, eq 4, obtained at $E^* = -232$ mV, $A = 1.97 \times 10^{-5}$ V²/(J·mol), $B = -1.33 \times 10^{-3}$ V²/K, and $C = 1.00$ V². The data shown were obtained in four experiments. Two of them were carried out at $T = 16$ °C (see Figure 2). In the third, $[Br^-]$ and $[HV^{2+}]$ were kept constant at 0.08 M and 2 mM, respectively, and T was changed over the range 16–40 °C. In the fourth, $[Br^-]$ and $[HV^{2+}]$ were fixed at 0.04 M and 2 mM, respectively, while T was varied from 16 to 30 °C. E_C^0 and E_G^0 values are denoted by the symbols \circ and \square , respectively.

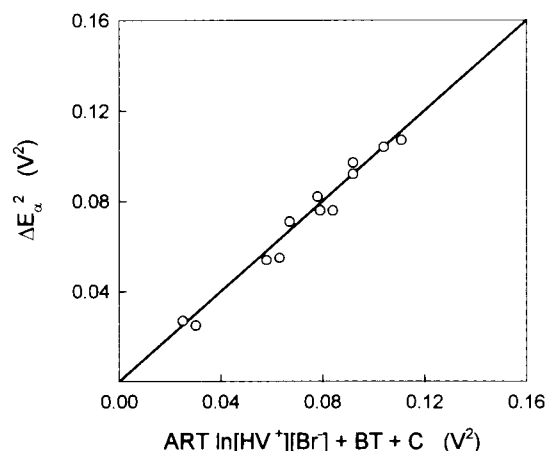
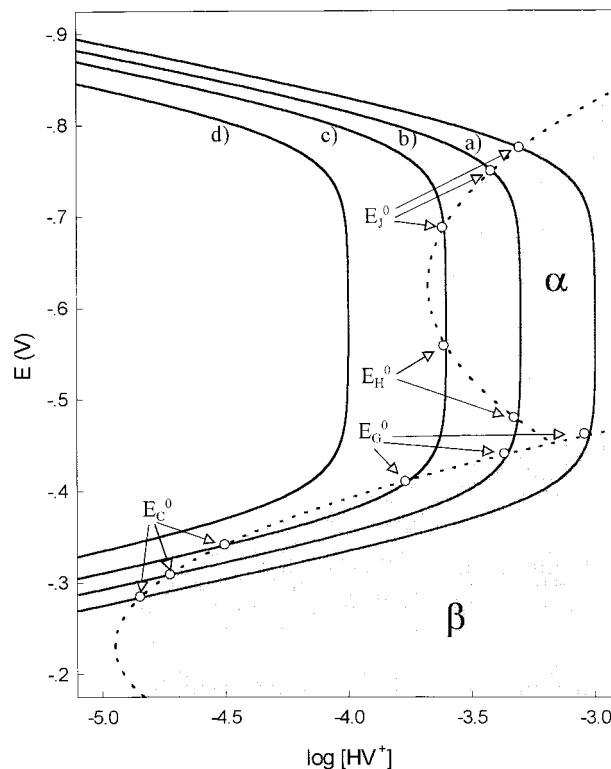


Figure 8. Plots of $(\Delta E_\alpha)^2$ vs $\{ART \ln([HV^{2+}][Br^-]) + BT + C\}$. $(\Delta E_\alpha)^2$ values were obtained by measuring the distance between the peak potentials for peaks **H**₁ and **J**₁, as in Figures 5 and 6. The solid line represents the predictions of eq 2 with $A = 4.3 \times 10^{-5}$ V²/(J·mol), $B = -9.2 \times 10^{-3}$ V²/K, and $C = 3.7$ V².

for **J**₁ was more than 60 mV apart from the standard reduction potential for the HV^{•+}/HV couple (peak **L**), so the concentration of the cation radical around the electrode between peaks **H**₁ and **J**₁ could be assumed constant and equal to that of HV²⁺ in the bulk solution.

The previous factors significantly restrict the range of experimental conditions where eq 2 can be reliably tested with phase α . In any case, at the ΔE_α values that meet the above-described conditions, plots of $(\Delta E_\alpha)^2$ vs $\ln [HV^{2+}]$ at constant T and $[HV^{2+}]$ or $[Br^-]$ were found to be linear and have roughly the same slope. The global set of valid experiments was used to determine constants A , B , and C in eq 2 by numerical fitting of the experimental $(\Delta E_\alpha)^2$ values in the equation on the assumption that $[HV^{•+}] = [HV^{2+}]_B$. The values thus obtained were $A = (4.3 \pm 0.3) \times 10^{-5}$ V²/(J·mol), $B = (-9.2 \pm 0.9) \times 10^{-3}$ V²/K, and $C = 3.7 \pm 0.3$ V². Figure 8 shows a plot of $(\Delta E_\alpha)^2$ vs $\{ART \ln([HV^{•+}][Br^-]) + BT + C\}$ obtained by using the previous A , B , and C values.

SCHEME 3: Shaded Zones (α and β) Corresponding to the Regions Where the Two Phases Exist^a and Solid Lines Corresponding to the Predictions of Eq 7^b



^a The regions were determined by applying the method of Scheme 2 to the experimental A , B , C , and E^* values for each phase (see text), with $[Br^-] = 0.2$ M and $T = 16$ °C. ^b With $[HV^{2+}]_B = 3 \times 10^{-4}$ M (a), 5×10^{-4} M (b), 10^{-3} M (c), and 2×10^{-3} M (d). E_B^0 and E_L^0 were experimentally determined in each case, with $T = 16$ °C.

As can be seen, the plot was acceptably linear, so eq 2 was reasonably well satisfied. The maximum adsorption potential for this phase, E^* , was estimated to be -625 mV.

Conclusions

The results described in the previous sections suggest that phase β consists of a 1:1 mixture of HV^{•+} and Br⁻ where the concentration of the former is such that $\Gamma_\beta \approx 1.04 \times 10^{-10}$ mol/cm². This phase adsorbs HV²⁺ molecules, possibly in addition to Br⁻ ions.

From the previous results it also follows that phase α consists of a 1:1 mixture of HV^{•+} and Br⁻. In addition, the HV^{•+} concentration in this phase appears to be such that $\Gamma_\alpha \approx 2.08 \times 10^{-10}$ mol/cm² (the value obtained from the charge exchanged along peak **D**₁ in a water/DMSO medium with $X_{\text{DMSO}} < 0.75$).²⁴ Phase α was previously observed for HV^{•+} in an aqueous medium.^{22,24} This phase must have a very similar structure in both media; its stability, however, is higher in water than in DMSO. Thus, the critical condensation temperature, T^* , of phase α in an aqueous solution containing 0.1 mM HV²⁺ and 0.1 M KBr is ca. 82 °C.²² In DMSO, T^* can be calculated by taking $(\Delta E_\alpha)^2 = 0$ in eq 2 and solving it for T . By using the same concentrations and the previously calculated A , B , and C values, T^* was found to be about 25 °C.

By way of example, Scheme 3 shows the $\log [HV^{2+}]$ vs E phase diagram obtained at $[Br^-] = 0.1$ M at $T = 16$ °C. The shaded zones, α and β , correspond to the regions where each phase occurs. Such regions were identified by using eq 2 with the previous A , B , C , and E^* values.

The solid line in Scheme 3 represents the variation of $\ln [HV^{*+}]$ with E as per eq 3 at different $[HV^{2+}]_B$ values and the experimental E_B^0 and E_L^0 values. The points where the solid lines intersect the shaded areas in the scheme indicate the positions of the potentials E_C^0 , E_G^0 , E_H^0 , and E_J^0 , which bound the apparent regions of existence of the phases in terms of the variable concentration of the cation radical on the electrode surface.

Acknowledgment. The authors wish to express their gratitude to Spain's DGICYT for funding this research within the frameworks of Projects PB94-0448 and PB97-0453.

References and Notes

- Retter, U.; Lohse, H. *J. Electroanal. Chem.* **1982**, *134*, 243.
- Sridharan, R.; De Levie, R.; Rangarajan, S. K. *Chem. Phys. Lett.* **1987**, *142*, 43.
- Nikitas, P.; Andoniou, S. *J. Electroanal. Chem.* **1994**, *375*, 339.
- Pushpalatha, K.; Sangaranarayanan, M. V. *J. Electroanal. Chem.* **1997**, *425*, 39.
- Baikerikar, K. G.; Sathyanarayana, S. J. *J. Electroanal. Chem.* **1970**, *24*, 333.
- Dyatkina, S. L.; Damaskin, B. B.; Fedorovich, N. V.; Stenina, E. V.; Yusupova, V. A. *Elektrokhimiya* **1972**, *9*, 1283.
- Retter, U. *J. Electroanal. Chem.* **1984**, *165*, 221; **1987**, *236*, 21.
- Philipp, R.; Retter, U.; Dittrich, J.; Müller, E.; Kuschel, F. *Electrochim. Acta* **1987**, *32*, 1671.
- De Levie, R. *Chem. Rev.* **1988**, *88*, 599.
- Wandlowski, Th.; Chaiyasith, P.; Baumgärtl, H. *J. Electroanal. Chem.* **1993**, *346*, 271.
- Wandlowski, Th.; De Levie, R. *J. Electroanal. Chem.* **1993**, *349*, 15.
- Jelen, F.; Vettlerl, V.; Schaper, A.; Jovin, T.; Paleček, E. *J. Electroanal. Chem.* **1994**, *377*, 197.
- Wandlowski, Th. *J. Electroanal. Chem.* **1995**, *395*, 83.
- Prieto, I.; Martín, M. T.; Muñoz, E.; Camacho, L. *J. Phys. Chem.* **1995**, *99*, 14083.
- Wandlowski, Th.; Höllzle, M. H. *Langmuir* **1996**, *12*, 6604.
- Wandlowski, Th.; Geoffrey, B. J.; De Levie, R. *J. Phys. Chem.* **1993**, *97*, 10119.
- Scharifker, B.; Wehrmann, C. *J. Electroanal. Chem.* **1985**, *185*, 93.
- Heyrovsky, M.; Novotny, L. *Collect. Czech. Chem. Commun.* **1987**, *52*, 1097.
- Sánchez-Maestre M.; Rodríguez-Amaro, R.; Muñoz, E.; Ruiz, J. J.; Camacho, L. *J. Electroanal. Chem.* **1993**, *359*, 325.
- Sánchez-Maestre M.; Rodríguez-Amaro, R.; Muñoz, E.; Ruiz, J. J.; Camacho, L. *Langmuir* **1994**, *10*, 723.
- Salas, R.; Sánchez-Maestre M.; Rodríguez-Amaro, R.; Muñoz, E.; Ruiz, J. J.; Camacho, L. *Langmuir* **1995**, *11*, 1791.
- Millán, J. I.; Sánchez-Maestre, M.; Camacho, L.; Ruiz, J. J.; Rodríguez-Amaro, R. *Langmuir* **1997**, *13*, 3860.
- Kelaidopoulou, A.; Kokkinidis, G.; Coutouli-Argyropoulou, E. *Electrochim. Acta* **1998**, *43*, 987.
- Millán, J. I.; Rodríguez-Amaro, R.; Ruiz, J. J.; Camacho, L. *Langmuir* **1999**, *15*, 618.
- Cotton, T. M.; Lu, T.; Uphaus, R. A. *Microchem. J.* **1990**, *42*, 44.
- Lu, T.; Cotton, T. M.; Birke, R. L.; Lombardi, J. R. *Langmuir* **1989**, *5*, 406.
- Bird, C. L.; Huhn, A. T. *Chem. Soc. Rev.* **1981**, *10*, 49.
- Sánchez-Maestre M.; Rodríguez-Amaro, R.; Muñoz, E.; Ruiz, J. J.; Camacho, L. *J. Electroanal. Chem.* **1994**, *373*, 31.
- Prieto, I.; Martín, M. T.; Muñoz, E.; Ruiz, J. J.; Camacho, L. *J. Electroanal. Chem.* **1997**, *424*, 113.
- Demir, U.; Shannon, C. *Langmuir* **1996**, *12*, 6091.
- Hatchett, D. W.; Uibel, R. H.; Stevenson, K. J.; Harris, J. M.; White, H. S. *J. Am. Chem. Soc.* **1998**, *120*, 1062.
- Fleischmann, M.; Thirst, H. R. In *Advances in Electrochemistry and Electrochemical Engineering*; Delahay, P., Ed.; Interscience: New York, 1963; Vol. 3.
- Harrison, J. A.; Thirst, H. R. In *Electroanalytical Chemistry*; Bard, A. J., Ed.; Marcel Dekker: New York, 1977; Vol. 5, p 67.
- Brdička, R. Z. *Elektrochem.* **1942**, *48*, 278.